



Ruthenium-induced hydrolysis effect on Fe_2O_3 nanoarrays for high-performance electrochemical nitrate reduction to ammonia



Shumin Luo ^{a,b}, Heng Guo ^{a,b,*}, Tingsong Li ^{a,b}, Haoran Wu ^{a,b}, Fengying Zhang ^{a,b}, Chun Tang ^{a,b}, Guoxing Chen ^c, Guidong Yang ^d, Ying Zhou ^{a,b,*}

^a State Key Laboratory of Oil and Gas Reservoir Geology and Exploitation, Southwest Petroleum University, Chengdu 610500, China

^b School of New Energy and Materials, Southwest Petroleum University, Chengdu 610500, China

^c Fraunhofer Research Institution for Materials Recycling and Resource Strategies IWKS, Brentanstraße 2a, Alzenau 63755, Germany

^d XJTU-Oxford International Joint Research Laboratory of Catalysis, School of Chemical Engineering and Technology, Xi'an Jiaotong University, Xi'an 710049, China

ARTICLE INFO

Keywords:

Electrochemical nitrate reduction
Ferric oxide
Hydrogenation
Hydrolysis effect

ABSTRACT

Electrochemical nitrate reduction (NO_3RR) to ammonia (NH_3) has become an attractive pathway for sewage remediation and ammonia synthesis. However, the NO_3^- electroreduction reaction remains hindered by the sluggish multi-proton involved steps without sufficient proton supply. Herein, we designed Ru nanoparticles (NPs) loaded onto ferric oxide nanoarrays ($\text{Ru}-\text{Fe}_2\text{O}_3$) catalysts with hydrolysis effect for high-efficient NH_3 production. $\text{Ru}-\text{Fe}_2\text{O}_3$ exhibits an impressive ammonia yield and faraday efficiency ($209\text{--}329\text{ }\mu\text{mol cm}^{-2}\text{ h}^{-1}$ and $45.2\text{--}72.8\%$, respectively). Ru-induced hydrolysis promotes the hydrogenation of the reaction intermediates in the process ($\text{H}_2\text{O} + \text{e}^- \rightarrow \text{H}^* + \text{OH}^-$) by accelerating the generation of localized protons at the reactive sites. More importantly, this effect can further accelerate the H^* -mediated indirect reduction pathway and the electron-mediated direct reduction pathway. These findings underscore the importance of relating NO_3RR performance with nanometallic particles-supported electrodes to advance catalyst design and operation.

1. Introduction

Ammonia (NH_3) serves as a key intermediate in the production of nitrogenous fertilizers and also has a high energy density, implying its significance for both food security and clean energy storage [1–6]. The Haber-Bosch (H-B) process, developed in 1905, remains the primary industrial method for synthesizing NH_3 , but it involves the costly use of high temperatures ($300\text{--}500^\circ\text{C}$) and pressures (200–300 bar) and produces vast quantities of carbon dioxide (CO_2) as a byproduct [7–12]. The nitrate (NO_3^-) reduction reaction shows promise as an electrocatalytic technique for synthesizing ammonia under ambient temperature and pressure conditions owing to the lower bond dissociation energy of the $\text{N}=\text{O}$ double bond (204 kJ/mol) compared to the $\text{N}\equiv\text{N}$ triple bond (941 kJ/mol) [13,14]. The wide availability of NO_3^- in the aqueous phase further renders this system attractive as an alternative to the gas-liquid-solid system of the nitrogen reduction reaction (NRR) [8,15,16]. However, the efficiency of the electrochemical nitrate reduction (NO_3RR) process is currently not adequate due to the complications arising from the eight-electron oxidation process and its slow kinetic

rate, as well as competing side reactions and the hydrogen evolution reaction (HER) [4,17]. It is thus necessary to create robust catalysts with a strong activity that will boost the NO_3^- -to- NH_3 pathway while subduing any undesirable side products and HER processes [5,18–22].

The water-splitting process, which underlies the HER, plays a critical role in accelerating the kinetics of NO_3RR by supplying protons (H^*) as the essential hydrogen source needed for hydrogenating intermediates in the NO_3RR pathway. The optimization of the H_2O dissociation reaction to facilitate H^* production while inhibiting the combination of H^* to form H_2 is paramount for improving the rate of NO_3RR hydrogenation [23]. Yu's team created oxygen-doped Ru nanoclusters to show how tensile stresses induced by oxygen-dopant promote H^* production but hinder H^* dimerization during water splitting [24]. A higher concentration of H^* radicals facilitates the hydrogenation of NO_3^- through the NO_3RR pathway, leading to an enhanced rate of NH_3 production. The study by Yin et al. found that the electronic coupling between Au and Cu within an Au_1Cu (111) single-atom-alloy catalyst generated electron-deficient Cu active sites. This gave rise to two effects: the rate of H_2O dissociation was enhanced, while the rate of H^* dimerization was

* Corresponding authors at: State Key Laboratory of Oil and Gas Reservoir Geology and Exploitation, Southwest Petroleum University, Chengdu 610500, China.
E-mail addresses: heng.guo@swpu.edu.cn (H. Guo), yzhou@swpu.edu.cn (Y. Zhou).

reduced. The combined effects were that the NO_3^- hydrogenation kinetics were sped up, leading to an increased production of NH_3 [2]. The search for new NO_3^- RR catalysts that can activate both the dissociation of NO_3^- and H_2O while properly guiding the produced H^* towards the intermediate hydrogenation during the NO_3^- RR process was inspired by these positive results. However, when considering the mechanism of the electrocatalytic nitrate reduction reaction, further research is needed to understand the mechanism by which active hydrogen participates in the nitrate reduction reaction.

It is essential for the design of such catalysts to have a basic comprehension of the movement and interaction of generated H^* radicals with reaction intermediates. In previous studies, non-metallic materials have been recognized for their advantages of low cost, high mechanical strength, tunable electronic structures, and significant durability [25]. However, they often suffer from inadequate intrinsic activity and slow kinetic rates in electrocatalytic applications [26]. Single-atom catalysts, with their simple structure and homogeneity, contribute to the rational design of catalysts [27,28]. However, the effective synthesis of single-atom catalysts with simultaneous improvement of NH_3 yield still poses challenges. Cu-based materials are widely used for nitrate reduction due to their low cost and abundant availability [29]. However, they exhibit relatively poor electrocatalytic activity and selectivity. Additionally, their long-term durability needs to be further improved [30,31]. Recently, Ru-based catalysts have been found to possess a strong hydrogen bond strength similar to Pt, as well as a cost-effectiveness advantage, which has generated particular interest [32,33]. Furthermore, the element Ru has been observed to possess an extraordinary capacity to facilitate aqueous dissociation [34]. The dispersal of noble metals on a carrier material having a high specific surface area can dramatically decrease costs and boost catalytic sites. Iron oxide (Fe_2O_3) can be exploited due to its naturally abundant occurrence in nature, its thermodynamic stability, and its affordability. More importantly, some studies have indicated that Fe_2O_3 presents a successful adsorption rate of nitrate [35]. Hence, Ru element-modified Fe_2O_3 can incite water dissociation, potentially providing more H^* to boost the nitrate reduction activity.

Herein, we reported the use of ruthenium nanoparticles loaded on iron oxide ($\text{Ru-Fe}_2\text{O}_3$) as high-efficient catalysts for the conversion of nitrate to ammonia product. The introduction of Ru nanoparticles (Ru NPs) located at Fe_2O_3 nanoarrays favors the formation of more reaction actives for hydrolysis and nitrate hydrogenation. This effect results in a 57% enhancement of the NH_3 yield and a 61% enhancement of Faraday efficiency. Electron paramagnetic resonance (EPR), electrochemical online differential electrochemical mass spectrometry (DEMS), in situ attenuated total reflection surface-enhanced infrared absorption spectroscopy (ATR-SEIRAS), and density functional theory (DFT) calculations results further demonstrate the reaction pathways and conversion mechanisms from NO_3^- to NH_3 with the activation and dissociation of $\text{NO}_3^-/\text{H}_2\text{O}$ by ruthenium-induced hydrolysis effect.

2. Experimental

2.1. Synthesis of Fe_2O_3

0.24 g 6 $\text{H}_2\text{O}\text{-FeCl}_3$ and 0.4 g Na_2SO_4 were dissolved into 35 mL ultrapure water. The above solution and a piece of cleaned carbon cloth ($2 \times 3 \text{ cm}^2$) were transferred to a 50 mL Teflon-lined stainless-steel autoclave. After sealing the autoclave, it was placed in an oven at 120 °C for 6 h, followed by natural cooling. The resulting precursor (FeOOH) supported on carbon cloth was washed repeatedly and then dried at 60 °C. After annealing at 450 °C for 3 h under an Ar atmosphere, a Fe_2O_3 sample was obtained.

2.2. Synthesis of $\text{Ru-Fe}_2\text{O}_3$

To prepare $\text{Ru-Fe}_2\text{O}_3$, an impregnation solution was first prepared by

dissolving $\text{RuCl}_3\text{-xH}_2\text{O}$ into 10 mL of ethanol under magnetic stirring. A piece of carbon cloth supported by FeOOH ($2 \times 3 \text{ cm}^2$) was dipped into the impregnation solution for 10 min and was subsequently taken out and dried under 60 °C. After annealing at 450 °C for 3 h under an Ar atmosphere, $\text{Ru-Fe}_2\text{O}_3$ sample was obtained. Concurrently, a range of $\text{Ru-Fe}_2\text{O}_3$ samples was synthesized by adding varying quantities of $\text{RuCl}_3\text{-xH}_2\text{O}$, which were used to prepare precursor solutions with various concentrations. The $\text{Ru-Fe}_2\text{O}_3$ samples synthesized by adding 5, 10, and 20 mg of $\text{RuCl}_3\text{-xH}_2\text{O}$ were named 500, 1000, and 2000 ppm $\text{Ru-Fe}_2\text{O}_3$, respectively.

2.3. Electrochemical nitrate reduction measurements

An electrochemical workstation (CHI760, Chenhua, Shanghai) was employed to conduct all electrochemical tests. In the experiments, a three-electrode system was employed, where $\text{Ru-Fe}_2\text{O}_3$ electrodes served as the working electrode, a stone grinding rod acted as the counter electrode, and Ag/AgCl electrodes were implemented as the reference electrode. The electrolyte is 0.5 M Na_2SO_4 with or without 0.1 M NaNO_3 . All of the potentials were reported relative to the reversible hydrogen electrode (RHE) after conversion ($E_{\text{RHE}} = E_{\text{Ag/AgCl}} + 0.518 \text{ V}$). A scan rate of 10 mV/s was used to collect the linear sweep voltammetry (LSV) curves. To calculate the electrocatalytic surface area (ECSA), cyclic voltammetry (CV) tests were performed at different scanning speeds within the non-Faraday reaction potential. Electrochemical impedance spectroscopy (EIS) was employed to collect impedance data over the frequency range of 10^5 Hz to 0.1 Hz. The reduction products in the solution were analyzed using a UV-vis spectrophotometer (UV-2600, Shimadzu). The gas products in solution were analyzed using a gas chromatograph (GC 7820 A, Agilent). All experiments were carried out under ambient temperature and pressure conditions.

For membrane electrode assembly (MEA) measurements, the production of ammonia by a catalyst with a large-area was measured using a flow cell. The reduction reaction would occur at the surface of the cathode ($\text{Ru-Fe}_2\text{O}_3$), while the oxidation reaction would take place at the surface of the anode (NF), and the surface area of both reactions is $2 \times 2 \text{ cm}^2$. A solution containing 0.1 M NaNO_3 and 0.5 M Na_2SO_4 (120 mL in total) was utilized, with an equal volume divided between the two solution reservoirs. A peristaltic pump was connected to the solution reservoirs and electrolytic cell using a white hose to enable circulation of the electrolyte solution at a flow rate of 30 mL min^{-1} . In order to assess the catalytic performance of NO_3^- RR in NH_3 production, chronoamperometry tests were conducted over a duration of 0.5 h, employing a specific potential range of -2 to -4 V.

Chemicals and materials, catalyst characterization, determination of products, electrochemical online DEMS measurements, in situ ATR-SEIRAS measurements, and DFT computational details are described in [Supporting Information](#).

3. Results and discussion

3.1. Synthesis and characterization

Fe_2O_3 ($\text{Fe}_2\text{O}_3/\text{CC}$) and Ru-loaded Fe_2O_3 ($\text{Ru-Fe}_2\text{O}_3/\text{CC}$) were synthesized *in situ* on carbon cloth (CC) via a facile two-step hydrothermal route ([Fig. 1a](#)). X-ray diffraction (XRD) pattern of $\text{Ru-Fe}_2\text{O}_3$ ([Fig. 1b](#)) exhibits these patterns consistent with those of Fe_2O_3 (PDF #330664), and no characteristic peaks assigned to Ru and RuO_2 owing to the particles' small size and low content, suggesting that Ru species could be highly dispersed [36]. Scanning electron microscopy (SEM) images of Fe_2O_3 ([Fig. 1c](#) and [Fig. S1](#)) and $\text{Ru-Fe}_2\text{O}_3$ ([Fig. 1d](#) and [Fig. S2](#)) confirm the presence of an array of densely packed Fe_2O_3 nanorods on CC with a size of several hundred nanometers. The growth of Ru NPs leads to larger inter-electrode/reactant reaction surfaces, advantageous for electrocatalytic applications. In addition, elemental mapping ([Fig. 1e-i](#))

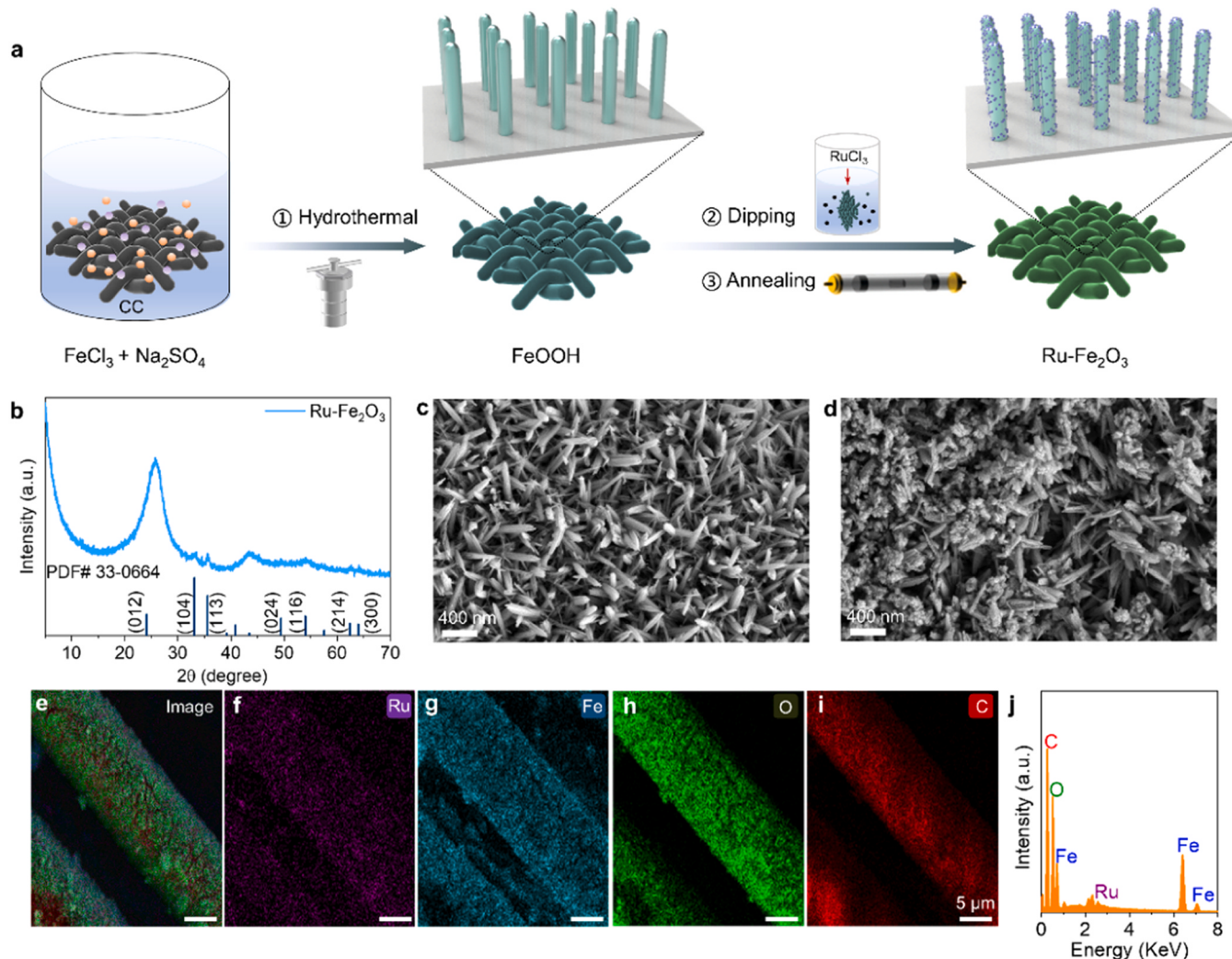


Fig. 1. a) Scheme for the preparation and electrocatalytic nitrate reduction of Ru-Fe₂O₃. b) XRD pattern of Ru-Fe₂O₃. SEM images of c) Fe₂O₃ and d) Ru-Fe₂O₃. e) Elemental mapping images of Ru-Fe₂O₃, f) Ru, g) Fe, h) O, and i) C. j) EDX spectrum of Ru-Fe₂O₃.

and energy-dispersive X-ray spectroscopy (EDX) spectrum (Fig. 1j) confirm the presence and uniform distribution of Ru species throughout the Fe₂O₃ nanorod arrays without obvious aggregation.

Transmission electron microscopy (TEM) images further confirm the nanoscale structure morphology of the as-prepared Ru-Fe₂O₃ as a nanoarray. As shown in Fig. 2a, the surface of the nanoarray is rougher with a width of nearly 40 nm, illustrating the presence of the abundant metallic Ru NPs on the Fe₂O₃ nanoarrays. The related high-resolution TEM (HRTEM) image indicates that the Ru NPs on the Ru-Fe₂O₃ supported catalyst are uniformly distributed, with the majority of particles having a diameter of approximately 2.43 ± 0.76 nm (Fig. 2b). As shown in Fig. 2c, the clear lattice stripes with a spacing of 0.214 nm observed in the nanoarrays through HRTEM analysis correspond to the (002) plane of Ru [37]. The selected area electron diffraction (SAED) result further confirms that the Ru-Fe₂O₃ have a polycrystalline structure (Fig. S3), pointing to the (110) face of Fe₂O₃ and the (011) face of Ru, respectively. EDX reveals the atomic ratio of Ru: Fe: O is 4: 46: 50 (Fig. S4), indicating the successful loading of Ru NPs onto the Fe₂O₃ nanoarrays. As shown in Table S1, the final Ru and Fe loading in Ru-Fe₂O₃ is about 0.01 wt% and 2.71 wt% based on ICP-AES analysis.

To identify the surface chemistry of the catalyst, an X-ray photoelectron spectroscopy (XPS) analysis was performed. The XPS survey spectra demonstrate the evidence of Ru, Fe, and O elements (Fig. S5). In Fig. 2d, the two peaks of the Ru 3d and C 1s spectra were centered at

280.3 and 281.1 eV, which are attributed to Ru 3d_{5/2} of Ru⁰ and Ru⁴⁺, respectively. The comparison between the areas indicates that the majority of Ru was present in the metallic state, with a fraction of the Ru being partially oxidized. Furthermore, the spectra's three peaks at 284.5, 285.3, and 288.3 eV were identified as C 1 s from carbon species [38]. The high-resolution spectra of Fe 2p in Fe₂O₃ and Ru-Fe₂O₃ are shown in Fig. 2e. Fig. 2e indicates the occurrence of Fe²⁺ ions at binding energies of 710.6 and 724.2 eV and Fe³⁺ ions at binding energies of 713.0 and 727.2 eV in Ru-Fe₂O₃, and the remaining two peaks belong to satellite peaks [39]. An energy shift of approximately 0.7 eV is observed for the Fe 2p_{3/2} peak of Ru-Fe₂O₃, in comparison to that of Fe₂O₃, suggesting electron transfer from Fe to Ru element. As shown in Fig. 2f, the O 1 s XPS patterns show three main peaks at 529.7, 530.4, and 531.7 eV, which belong to the lattice oxygen (O_{lat}), oxygen atoms in the vicinity of the oxygen vacancy (O_{vac}), and chemisorbed oxygen (O_{abs}), respectively [40–42]. The peak area of O_{vac} in Ru-Fe₂O₃ is higher, indicating a greater concentration of O_{vac}. It means that a high concentration of oxygen vacancies may serve as active sites for NO₃RR [43, 44].

3.2. Electrocatalytic performance

Based on the unique structure of noble metal nanoparticles supported on metal oxide, electrocatalytic NO₃RR measurements are

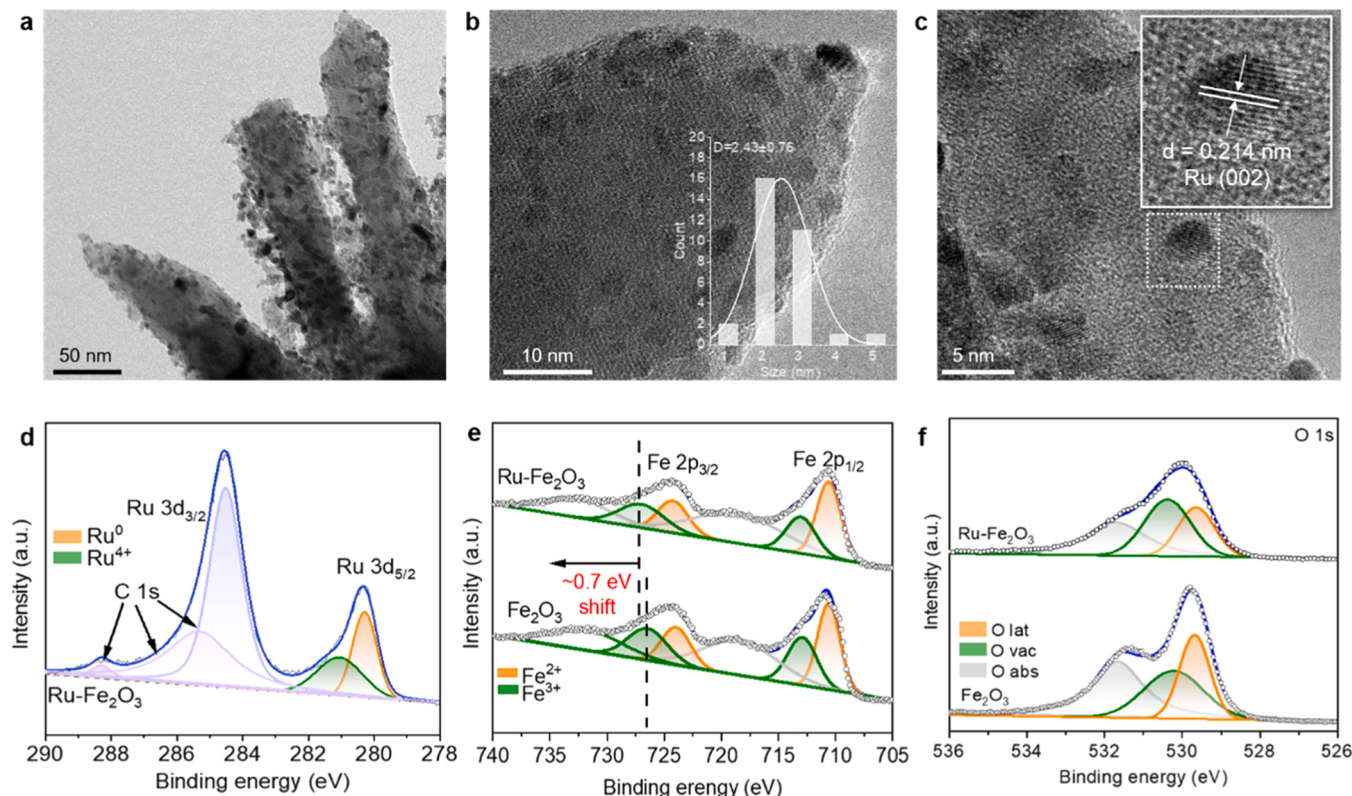


Fig. 2. a) TEM images. b-c) HRTEM images of Ru- Fe_2O_3 . High-resolution XPS spectra of d) Ru 3d orbital for Ru- Fe_2O_3 . High-resolution XPS spectra of e) Fe 2p orbital and f) O 1s orbital for Ru- Fe_2O_3 and Fe_2O_3 .

carried out in an H-type cell containing 0.1 M NaNO_3 and 0.5 M Na_2SO_4 (Fig. S6a). The linear sweep voltammetry (LSV) curves in Fig. 3a demonstrate that Ru- Fe_2O_3 and Fe_2O_3 yield a substantially greater current response in the presence of NO_3^- compared to without NO_3^- , confirming the high NO_3RR activity of Ru- Fe_2O_3 [45,46]. Fig. S6b displays the LSV curves of Ru- Fe_2O_3 samples with varying Ru³⁺ precursor concentrations. These curves demonstrate that higher Ru³⁺ precursor concentrations resulted in greater current densities for the samples. Then the performance of Ru- Fe_2O_3 and Fe_2O_3 were quantitatively determined through combined testing by chronoamperometry (electrolysis for 0.5 h) and colorimetric tests (Fig. S7-S8). The Ru- Fe_2O_3 sample with the highest concentration of Ru exhibits the highest ammonia yield and Faraday efficiency, thus 2000 ppm Ru- Fe_2O_3 was selected for further investigation based on the observed catalytic performance. Fig. S9 shows the i-t curves for the NO_3RR performance of Ru- Fe_2O_3 and Fe_2O_3 at various potentials. As depicted in Fig. 3b and Fig. 3c, Ru- Fe_2O_3 shows the highest FE of 72.8% with the corresponding NH₃ yield rate of 329 $\mu\text{mol cm}^{-2} \text{h}^{-1}$ (compared to the FE of 45.2% and corresponding NH₃ yield of 209 $\mu\text{mol cm}^{-2} \text{h}^{-1}$ for the Fe_2O_3 catalyst), indicating Ru active sites have some favorable impacts on the NO_3RR performance. In addition, other by-products of Ru- Fe_2O_3 at different voltages were detected. The FE of Ru- Fe_2O_3 at -0.9 V vs. RHE is 72.85% for NO_3^- to NH₃, 3.27% for NO_3^- to NO_2^- , and only 1.45% for H₂, suggesting a good ammonia selectivity for the whole reaction (Fig. S10-12). A variety of relevant catalysts for NH₃ production from NO_3^- reduction are listed in Table S2. Subsequently, the effects of the substrate carbon cloth (CC) and reaction conditions or the electrocatalyst itself on the ammonia yield were ruled out (Fig. S13). Furthermore, the stability is another critical parameter for evaluating the practical application of a catalyst. Fig. S14 and Fig. 3d depict the stable NO_3RR performance of Ru- Fe_2O_3 under long-term electrolysis and ten consecutive cycles, respectively. Electrolytic NO_3RR testing was additionally performed using a larger cell, as depicted in Fig. 3e and Fig. S15. The current

densities used for the chronopotentiometry measurements might range from 50 to 500 mA cm^{-2} (Fig. 3e). NH₃ yield was measured at various potentials based on the corresponding current. Fig. 3f exhibits a high NH₃ yield rate of 0.48 $\text{mmol cm}^{-2} \text{h}^{-1}$ at -4.0 V, suggesting a prospective and suitable industrial application performance of the large-area loaded metal nanoparticles catalyst.

3.3. Mechanism investigation

From a kinetic perspective, the reasons for the enhanced catalytic activity were analyzed. The Tafel slopes are related to the polarization of the electrode and serve as indicators of a blocked electrode process [47]. Fig. S16 shows the Tafel slope of $15.78 \text{ mV dec}^{-1}$ for Ru- Fe_2O_3 and $37.80 \text{ mV dec}^{-1}$ for Fe_2O_3 , revealing that Ru NPs lead to an increased production of adsorbed hydrogen and facilitates faster kinetics of NO_3RR . Furthermore, ECSA serves as a potent electrochemical characterization technique for quantifying the active site density of electrocatalysts [48,49]. After testing the capacitance current density of Ru- Fe_2O_3 and Fe_2O_3 with different scan rates (Fig. S17a-b), ECSA is calculated and shown in Fig. S17c. The two straight lines with different slopes indicate that the ECSA of Ru- Fe_2O_3 (4.74 mF cm^{-2}) is ≈ 4 times that of Fe_2O_3 (1.18 mF cm^{-2}). This difference in ECSA shows that the loading of Ru nanoparticles makes Ru- Fe_2O_3 have more reaction active sites. Electron transfer is a critical factor in electrocatalytic reduction since rapid electron transfer promotes the efficiency of the reduction process [50]. The electrochemical impedance values of Ru- Fe_2O_3 and Fe_2O_3 are presented in Fig. S17d, accompanied by their equivalent circuit diagram. Compared to Fe_2O_3 , Ru- Fe_2O_3 exhibits the lowest resistance in the tested electrolyte, indicating superior electrical conductivity and efficient electron transport.

The Bode plots in Fig. 4 reveal that at low frequency (0.01 Hz) and low potential (0 V), the phase angles of the Ru- Fe_2O_3 and Fe_2O_3 electrodes are approximately 70° . This phase behavior indicates pseudo-

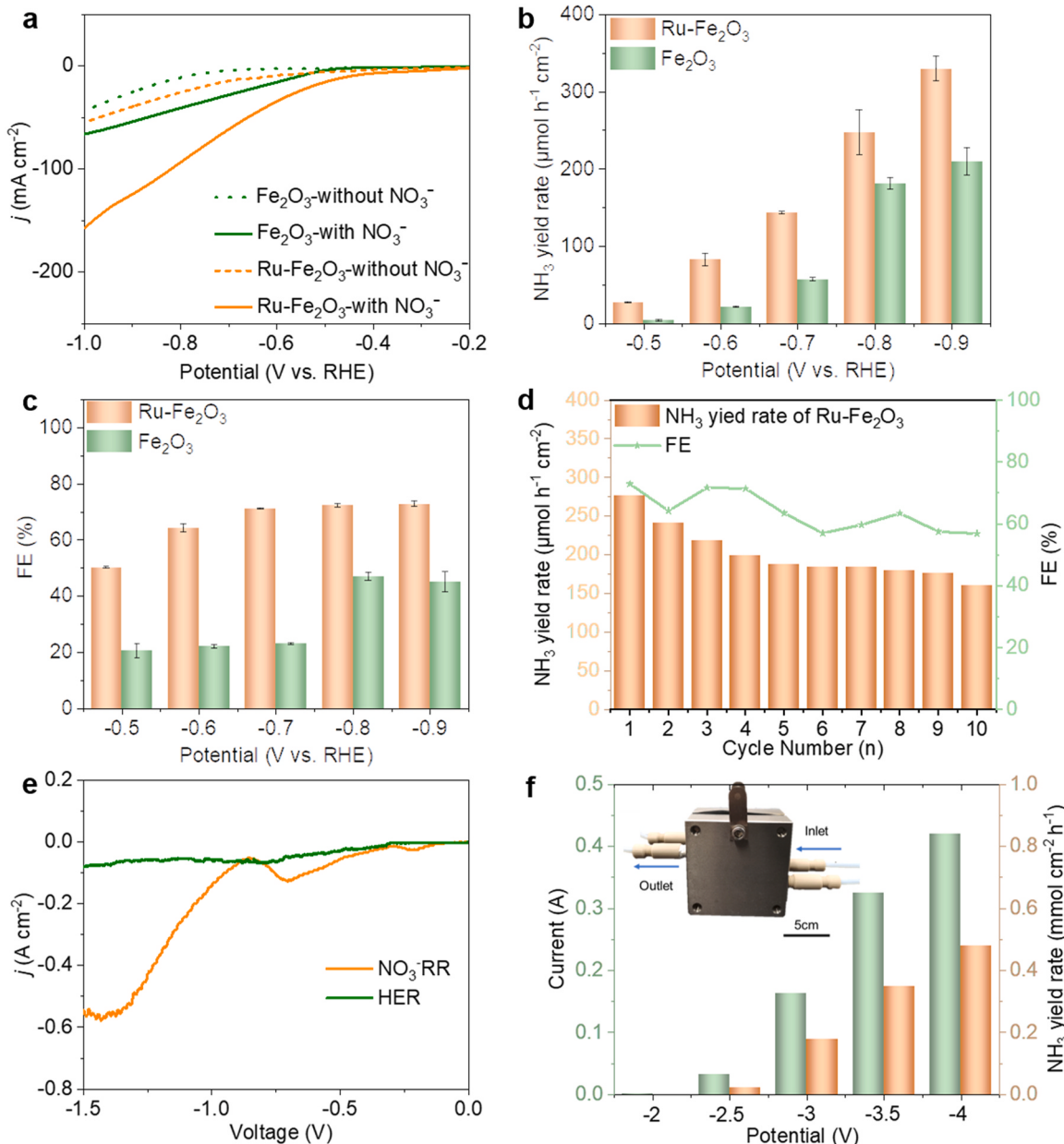


Fig. 3. Electrochemical ammonia production performance tests. a) LSV plots of Ru-Fe₂O₃ versus Fe₂O₃ with and without nitrate. b) NH₃ yield rates of Ru-Fe₂O₃ versus Fe₂O₃ and c) Faraday efficiency. d) NH₃ yield rates and FEs of Ru-Fe₂O₃ during the recycling tests at -0.8 V vs. RHE. e) LSV curves of HER and NO₃⁻RR over Ru-Fe₂O₃. f) NH₃ yield rates of the Ru-Fe₂O₃ electrode with large-area (2 × 2 cm²) at different given potentials.

capacitive characteristics arising from the interplay between mass and charge transfer resistances during electrode reactions [51]. As shown in Fig. 4a, a characteristic peak centered within the low-frequency region of 1–10 Hz appeared at -0.3 V after loading Ru NPs in a nitrate-free electrolyte. This peak shifted to higher frequencies and lower phase angles with increasing applied potential, which is associated with H* adsorption [52,53], whereas Fe₂O₃ at a higher voltage range in Fig. 4b depicted behavior indicates enhanced adsorption of H* with loading Ru NPs. As seen in Fig. 4c, the adsorption of H* disappeared over the same voltage range in the presence of NO₃, and a new kinetic process presented itself at -0.2 V after loading with Ru NPs, which is proposed to be due to the reduction of NO₃ at the interface of Ru-Fe₂O₃ resulting in its rapid adsorption on the surface of Ru-Fe₂O₃. The results of Fig. 4c-d indicated that the loading of Ru NPs resulted in comparable adsorption of *NO₃ at lower voltages compared to Fe₂O₃. Thus, it can be posited that the loading of Ru NPs increases the adsorption of both *NO₃ and H*.

The enhanced adsorption of *NO₃ and H* intermediates accelerate the hydrogenation processes hence promoting the NO₃⁻RR process.

The valence of the intermediates in the complicated process of NO₃⁻RR changes from +5 to -3. According to earlier research, an indirect H* mechanism and a direct electron mechanism are both involved in the electrocatalytic NO₃⁻RR process [54–57]. Since the hydrogenation process requires an adequate supply of protons, sufficient active protons or H* radicals are essential for efficient NO₃⁻RR. To assess the amount of H* radicals produced/consumed in the NO₃⁻RR process, liquid EPR measurements were performed using DMPO as an H* trapping reagent. The schematic diagram of the working principle of EPR is shown in Fig. 5a. As shown in Fig. 5b, In the absence of nitrate, EPR spectra revealed 9 signals with an intensity ratio of 1: 1: 2: 1: 2: 1: 2: 1: 1, indicating the generation of H* on both Ru-Fe₂O₃ and Fe₂O₃. Upon electrolysis with NO₃, the DMPO-H signals vanish entirely, indicating the rapid consumption of generated H* radicals in their contribution to

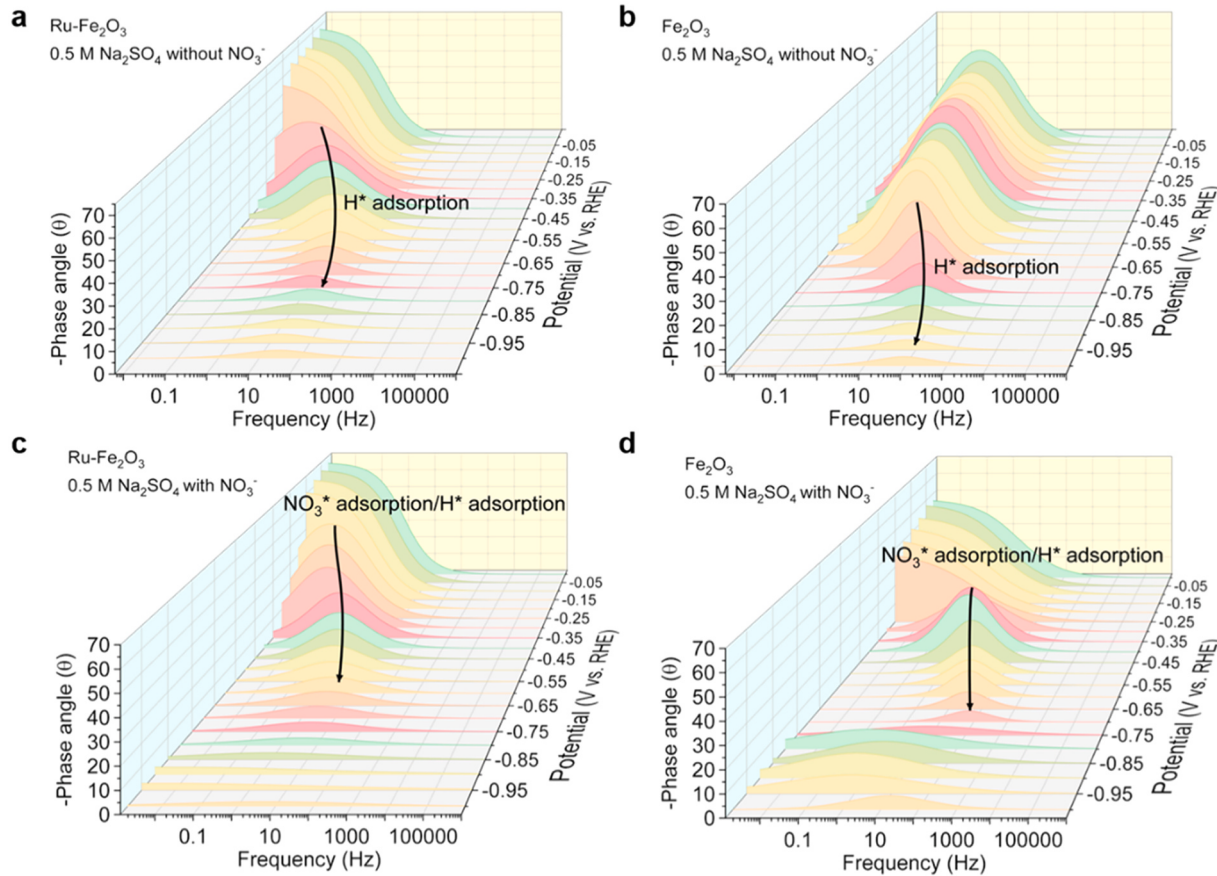


Fig. 4. Bode graphs of a) Ru-Fe₂O₃ and b) Fe₂O₃ measured in 0.5 M Na₂SO₄ at 0 ~ 1.05 V vs. RHE. Bode graphs of c) Ru-Fe₂O₃ and d) Fe₂O₃ measured in 0.5 M Na₂SO₄ with 0.1 M NaNO₃ at 0 ~ 1.05 V vs. RHE.

the hydrogenation reaction of NO₃RR. As shown in Fig. 5c-d, in nitrate-free electrolytes, the production of H* was observed to be greater in Ru-Fe₂O₃ than in Fe₂O₃ as time 0 passed from 5 min, suggesting that Ru can promote the production of H*. This can be attributed to the critical contribution of Ru which is known to be highly active for H₂O dissociation [58]. As shown in Fig. 5e-f, in the nitrate-containing electrolyte, liquid EPR measurements were carried out at 0, 1, and 5 min, respectively. The EPR intensity attenuation amplitude of Ru-Fe₂O₃ is significantly greater than that of Fe₂O₃, indicating the strong ability of Ru-Fe₂O₃ to consume H* and promote intermediate hydrogenation. This is why the yield and Faradaic efficiency of ammonia are higher than Fe₂O₃.

To gain a deeper understanding of the involvement of H* in the NO₃RR and the reaction pathway of the electrocatalytic process, we conducted electrochemical online DEMS and in situ ATR-SEIRAS spectroscopy. During the electrocatalytic NO₃RR, electrochemical online DEMS can identify the volatile intermediates and products that are formed. By measuring the signal intensity, it is possible to analyze the real-time concentration of the intermediates and products. The mass-to-charge ratio (*m/z*) signals captured as a function of time while executing constant potential polarization are shown in Fig. 6a-b. It should be noted that *m/z* signals were detected and monitored at 46, 31, 30, 17, and 16, corresponding to NO₂, HNO, NO, NH₃, and NH₂, respectively [15,59, 60]. Due to the instability of HNO, the detected signal is relatively weak. The conversion of NO to HNO is a proton-coupled electron transfer step ($*\text{NO} + \text{H}^+ + e^- \rightarrow *\text{HNO} + \text{OH}^-$), where protons are derived from the electrolyte [61]. Compared to Fe₂O₃, Ru-Fe₂O₃ exhibits a stronger HNO signal, possibly due to the promotion of H⁺ generation by the introduction of Ru NPs, leading to increased coverage of H on the surface of Ru-Fe₂O₃. The NH₃ and NH₂ signals of the Ru-Fe₂O₃ are about 1.17 and

1.21 times higher than those of the Fe₂O₃, respectively, which suggests that the introduction of Ru NPs facilitates the hydrogenation behavior of nitrate. Meanwhile, Ru-Fe₂O₃ shows a stronger NO₂ signal, indicating that the introduction of Ru NPs significantly facilitates the conversion of NO₃ to NO₂ in the decisive step, and more NO₂ participates in the subsequent hydrogenation reaction, which improves its ammonia production rate. Compared with Fe₂O₃, Ru-Fe₂O₃ exhibits both indirect reductions involving the key intermediate NH₂ and direct reduction involving the key intermediate HNO, indicating the occurrence of both indirect and direct reduction pathways in the NO₃RR reaction on Ru-Fe₂O₃, with indirect reduction dominating the reaction pathway [60, 61].

Moreover, in situ ATR-SEIRAS was performed to identify the intermediates in NO₃RR on different electrocatalysts as well. Fig. 6c and Fig. S18 were the results of in situ ATR-SEIRAS studying adsorption intermediates on Ru-Fe₂O₃. An increasing trend in the intensity of the NO₃ vibrational band at 1238 cm⁻¹ was observed as time progressed from 0 to 5 min, suggesting the continued consumption of NO₃ during the electrolysis of NO₃RR [62]. During the entire experiment, a broad peak exhibiting a tailing feature, centered around 3391 cm⁻¹, is identified as the NH₂ species [63]. The intensity of detected deoxidation intermediates (-NO₂ at 1624 cm⁻¹), hydrogenation intermediates (-NH₂OH at 1120 cm⁻¹, -NH₂ at 1179 cm⁻¹), and NH₃ (NH₄⁺ at 1451 cm⁻¹) progressively increased [23,64,65]. This indicates that Ru-Fe₂O₃ is capable of effectively activating NO₃ and generating a significant amount of hydrogenation intermediates, which are subsequently converted into NH₃. Due to the presence of NH₂ and NH₂OH, both indirect and direct reduction pathways occur in the NO₃RR reaction on Ru-Fe₂O₃, which is consistent with the DEMS results. Meanwhile, the H-O-H stretching vibration of H₂O (1651 cm⁻¹) was observed

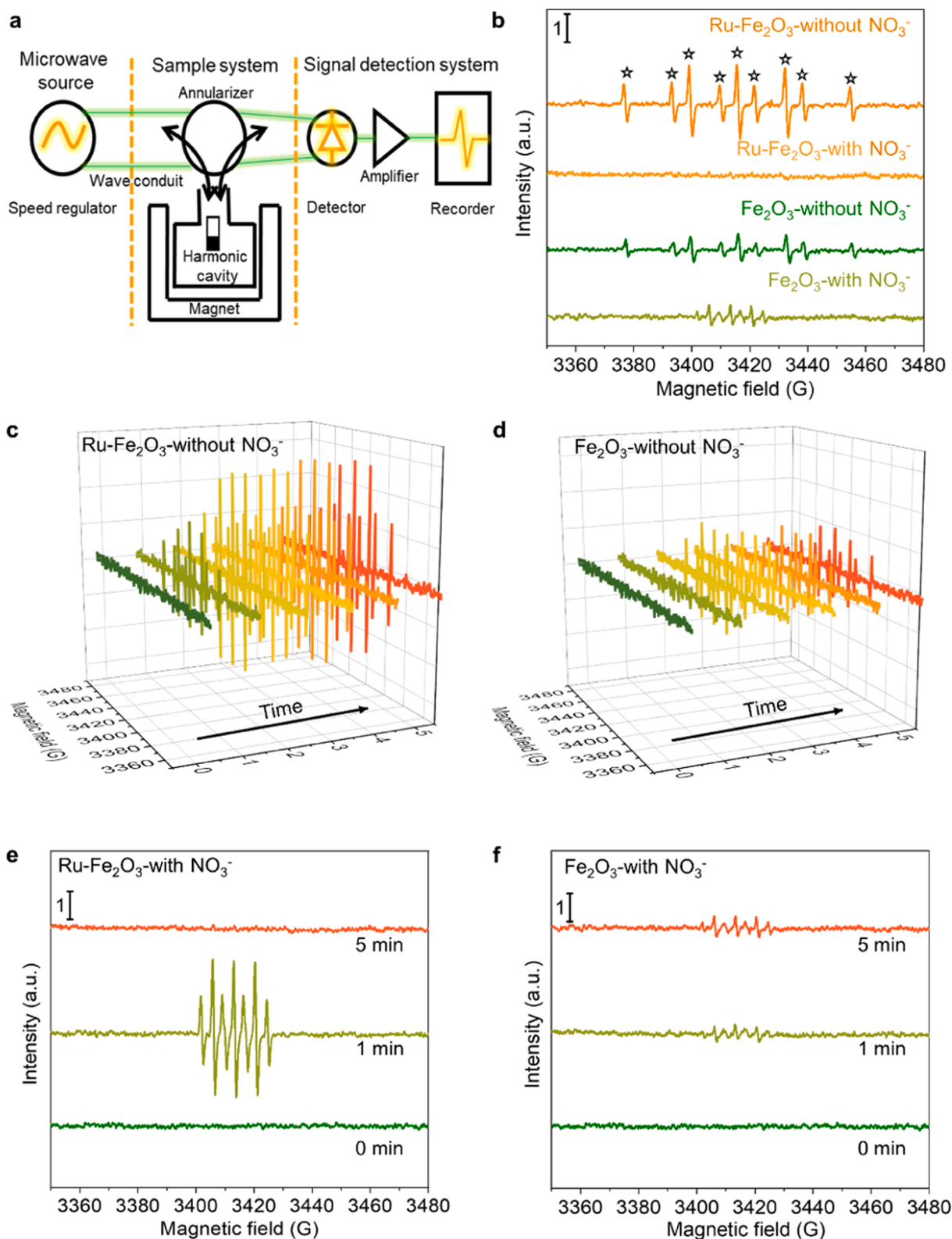


Fig. 5. a) The schematic diagram of the working principle of EPR. b) EPR spectra of DMPO participation of Ru-Fe₂O₃ and Fe₂O₃ under different electrolysis conditions. EPR spectra of c) Ru-Fe₂O₃ and d) Fe₂O₃ with DMPO participation under nitrate-free electrolyte at different electrolysis times. EPR spectra of e) Ru-Fe₂O₃ and f) Fe₂O₃ with DMPO participation under nitrate-containing electrolyte at different electrolysis times.

to be significantly enhanced during the NO₃RR process on Ru-Fe₂O₃, confirming the dissociation of H₂O into H⁺/OH⁻ stabilized on Ru-Fe₂O₃. Conversely, *in situ* ATR-SEIRAS spectrum of Fe₂O₃ (Fig. 6d) exhibits a limited presence of oxidation/hydrogenation intermediates, indicating

that its protonation reaction is relatively slow with fewer H^{*} species involved in the hydrogenation reaction, resulting in constrained NO₃RR kinetics and energetics of Fe₂O₃.

Based on electrochemical online DEMS and *in situ* ATR-SEIRAS, it

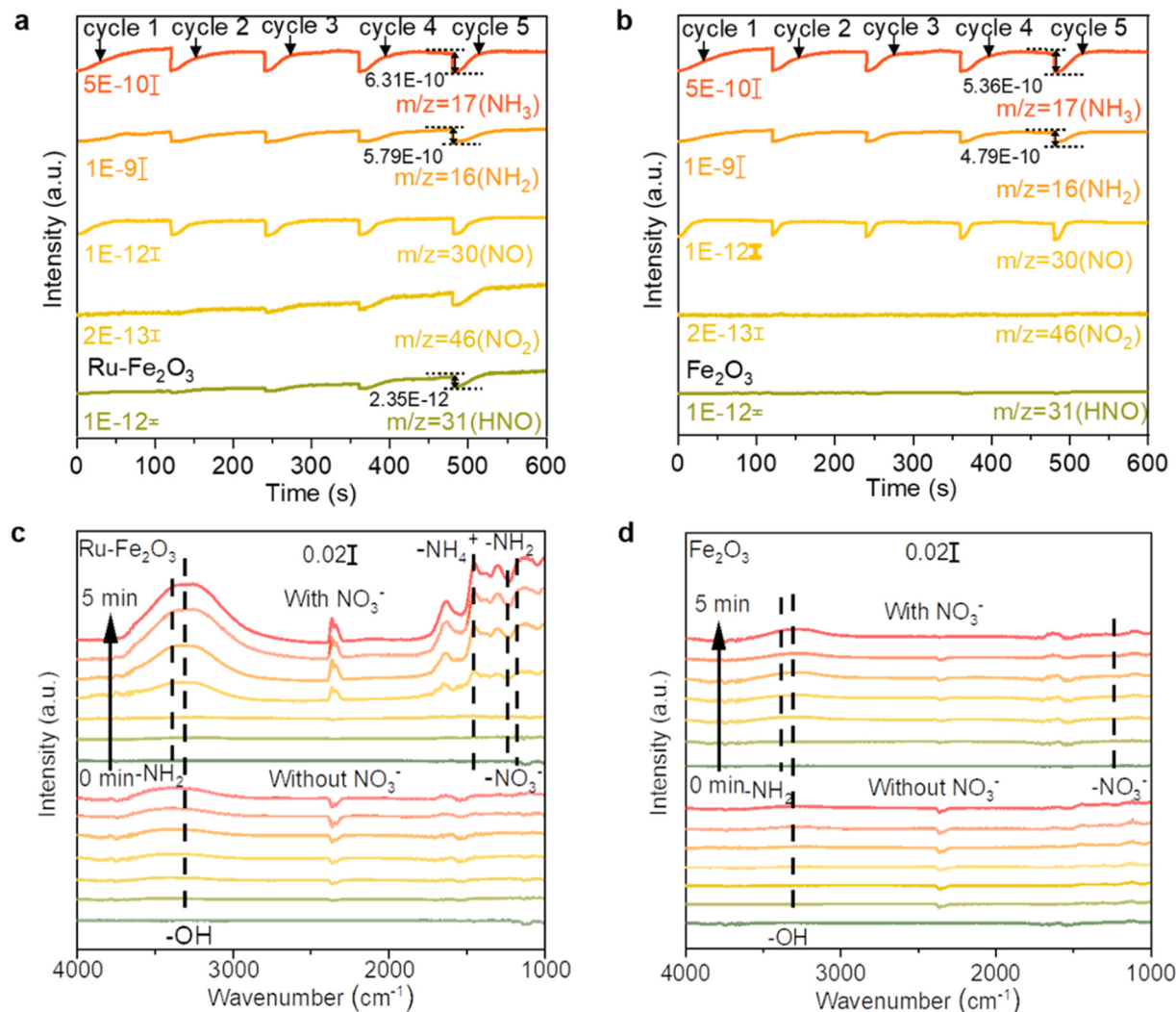


Fig. 6. DEMS measurements of NO_3RR over a) $\text{Ru-Fe}_2\text{O}_3$ and b) Fe_2O_3 . Time-resolved *in situ* electrochemical ATR-SEIRAS spectra over c) $\text{Ru-Fe}_2\text{O}_3$ and d) Fe_2O_3 at -0.8 V vs. RHE.

can be concluded that the introduction of Ru NPs can effectively promote the water dissociation reaction, leading to the generation of H^+/H^* species, and accelerating the protonation reactions in both indirect and direct reduction pathways. Furthermore, the electrocatalytic NO_3RR pathway of $\text{Ru-Fe}_2\text{O}_3$ is proposed to be the following: First, NO_3 is adsorbed on the $\text{Ru-Fe}_2\text{O}_3$, which gets reduced to $^*\text{NO}_2$ by electrochemistry. Subsequently, NO_2 rapidly converted to $^*\text{NO}$ through various reaction pathways. In pathway one, the reduction of $^*\text{NO}$ involves electron mediation, resulting in the formation of $^*\text{HNO}$, followed by hydrogenation and ultimately yielding $^*\text{NH}_3$. In pathway two, the reduction of NO occurs through hydrogen mediation, leading to the formation of $^*\text{N}$, which then undergoes hydrogenation to produce $^*\text{NH}_3$.

In order to provide a more comprehensive understanding of the reaction pathways occurring on the catalyst surface and the adsorption behavior of intermediate species. The front view and top view of the $\text{Ru-Fe}_2\text{O}_3$ computational model are shown in Fig. S19. The Gibbs free energy for each reaction step was calculated for $\text{Ru-Fe}_2\text{O}_3$ and Fe_2O_3 (Fig. 7a-b). It was found that the catalytic active sites of NO_3RR are Fe atoms near the $\text{Ru-Fe}_2\text{O}_3$ interface. The initial step is the adsorption of NO_3 , which can be viewed as the rate-determining step (RDS), and the Gibbs free energy suggests that this step is more favorable on $\text{Ru-Fe}_2\text{O}_3$ (2.17 eV) than that on Fe_2O_3 (4.71 eV). It implies the stronger adsorption of $^*\text{NO}_3$ on $\text{Ru-Fe}_2\text{O}_3$, which reveals that the introduction of Ru into Fe_2O_3 enhances the nitrate adsorption on the Fe surface and ensures the

occurrence of subsequent reactions. After that, $^*\text{NO}_3$ reacts with protons and electrons continuously to form $^*\text{NO}_2$ and $^*\text{NO}$. It is worth noting that for $\text{Ru-Fe}_2\text{O}_3$, there are two pathways for the electroreduction reaction to occur after $^*\text{NO}$ generation. Since $^*\text{NO}$ -to- $^*\text{N}$ on $\text{Ru-Fe}_2\text{O}_3$ is a heat-absorbing process, it is thermodynamically more favorable. The H^* -mediated indirect reduction pathway is more likely to occur, which is consistent with the DEMS results. As the reaction proceeds, the nitrate hydrogenation of $\text{Ru-Fe}_2\text{O}_3$ proceeds very smoothly, with few thermodynamic reaction barriers. On the contrary, Fe_2O_3 needs to overcome an energy barrier of 0.94 eV in the $^*\text{N}$ -to- $^*\text{NH}$ step, which proves that $\text{Ru-Fe}_2\text{O}_3$ favors the hydrogenation process, which is consistent with the DEMS results. Furthermore, the free energy diagrams depicting the hydrogen evolution reaction (HER) of both $\text{Ru-Fe}_2\text{O}_3$ and Fe_2O_3 were computed and presented in Fig. 7c. A greater H^* retention capacity can be inferred from the higher energy barrier observed during the H^* -to- H_2 transition on $\text{Ru-Fe}_2\text{O}_3$. The generated H^* exhibits limited release capability for H_2 formation, indicating effective inhibition of the HER and improved performance for the NO_3RR in the as-synthesized material. The computational simulation results further support the experimental findings.

4. Conclusions

In conclusion, this study demonstrates that the role of Ru NPs

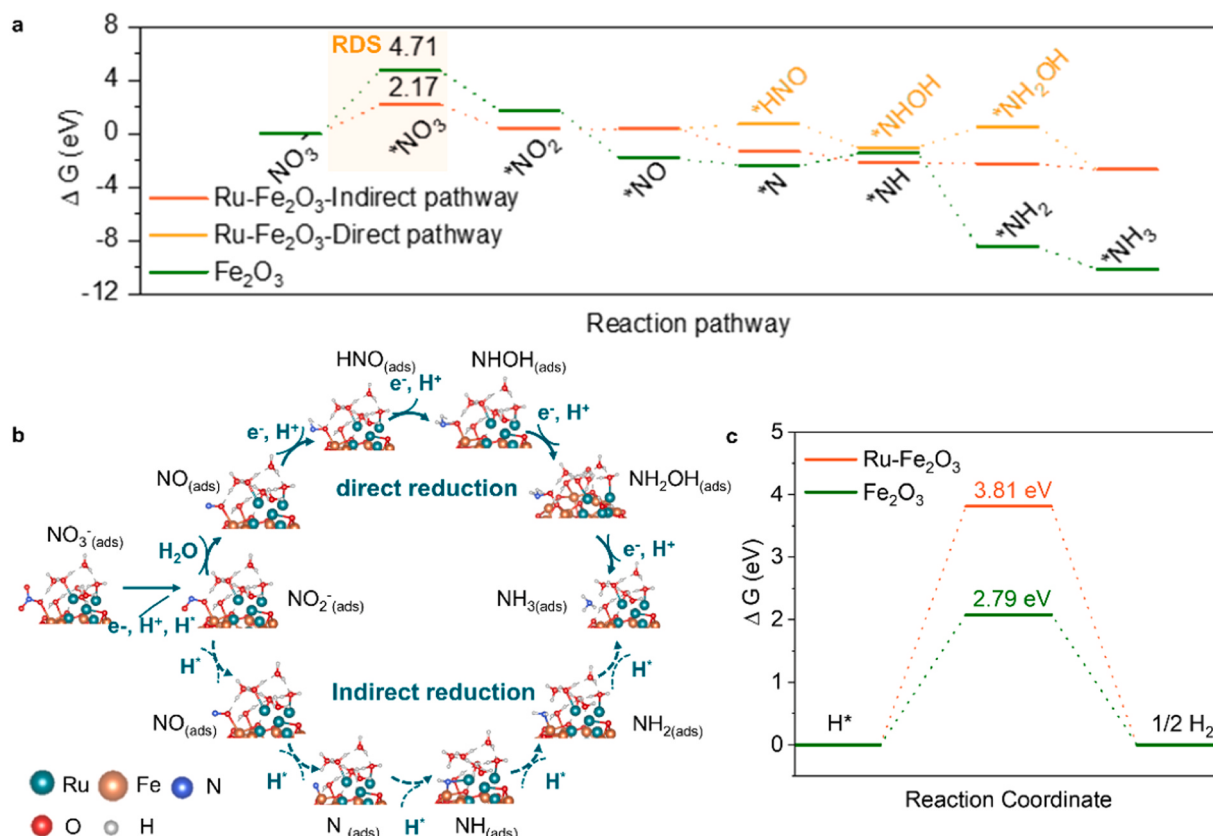


Fig. 7. a) Free energy of NO_3RR on Ru- Fe_2O_3 and Fe_2O_3 surface. b) The reaction pathway for Ru- Fe_2O_3 in the electrocatalytic NO_3RR . c) Gibbs free energy changes for the hydrogen-reduction reaction on Ru- Fe_2O_3 and Fe_2O_3 .

introduction during the NO_3RR process can greatly promote the ammonia production efficiency by Ru-induced hydrolysis effect. An impressive ammonia yield rate of $329 \mu\text{mol cm}^{-2} \text{h}^{-1}$ is achieved with a high FE of 72.8%. The operando FTIR/DEMS/ESR characterizations combined with DFT calculations indicate that the hydrogenation of the intermediates in the hydrolysis process is promoted by accelerating the generation of localized protons at the active sites from Ru-induced hydrolysis effect. As results, the effect accelerates the H^* -mediated indirect reduction pathway and the electron-mediated direct reduction pathway. This research provides insight into the application of nanometallic particles on a metallic oxide as efficient NO_3RR catalysts, as well as an in-depth understanding of NO_3RR mechanisms, which can be utilized as guidance to design efficient NO_3RR catalysts for NH_3 electrosynthesis.

CRediT authorship contribution statement

Fengying Zhang: Writing – review & editing, Methodology. **Haoran Wu:** Visualization, Software, Methodology. **Guoxing Chen:** Writing – review & editing. **Chun Tang:** Writing – review & editing, Methodology. **Shumin Luo:** Writing – original draft, Software, Methodology, Investigation. **Ying Zhou:** Writing – review & editing, Supervision, Resources, Funding acquisition, Conceptualization. **Tingsong Li:** Visualization, Methodology. **Heng Guo:** Writing – review & editing, Writing – original draft, Supervision, Funding acquisition, Formal analysis, Conceptualization. **Guidong Yang:** Writing – review & editing, Resources.

Declaration of Competing Interest

The authors declare that they have no known competing financial interests or personal relationships that could have appeared to influence the work reported in this paper.

Data availability

Data will be made available on request.

Acknowledgements

This work was supported by the National Key R&D Project of China (2020YFA0710000), National Natural Science Foundation of China (22109132), Provincial International Science and Technology Cooperation Project of Sichuan (24GJHZ0078), Provincial Key Research and Development Project of Sichuan (22SYSX0142 and 2021YFSY0046), International Science and Technology Cooperation Project of Chengdu (2021-GH02-00052-HZ), and Technology Innovation R&D Project of Chengdu (2022-YF05-00978-SN).

Appendix A. Supporting information

Supplementary data associated with this article can be found in the online version at [doi:10.1016/j.apcatb.2024.123967](https://doi.org/10.1016/j.apcatb.2024.123967).

References

- [1] Q. Gao, H. Pillai, Y. Huang, S. Liu, Q. Mu, X. Han, Z. Yan, H. Zhou, Q. He, H. Xin, H. Zhu, Breaking adsorption-energy scaling limitations of electrocatalytic nitrate reduction on intermetallic CuPd nanocubes by machine-learned insights, *Nat. Commun.* 13 (1) (2022) 12, <https://doi.org/10.1038/s41467-022-29926-w>.
- [2] Y. Zhang, X. Chen, W. Wang, L. Yin, J. Crittenden, Electrocatalytic nitrate reduction to ammonia on defective Au₁Cu (111) single-atom alloys, *Appl. Catal. B* 310 (2022) 121346, <https://doi.org/10.1016/j.apcatb.2022.121346>.
- [3] W. Gao, K. Xie, J. Xie, X. Wang, H. Zhang, S. Chen, H. Wang, Z. Li, C. Li, Alloying of Cu with Ru enabling the relay catalysis for reduction of nitrate to ammonia, 2202952, *Adv. Mater.* (2023) 1–9, <https://doi.org/10.1002/adma.202202952>.
- [4] J. Liang, Q. Liu, A. Alshehri, X. Sun, Recent advances in nanostructured heterogeneous catalysts for N-cycle electrocatalysis, *Nano Res. Energy* 1 (2022) 1–8, <https://doi.org/10.26599/nre.2022.9120010>.

[5] X. Cheng, J. He, H. Ji, H. Zhang, Q. Cao, W. Sun, C. Yan, J. Lu, Coordination symmetry breaking of single-atom catalysts for robust and efficient nitrate electroreduction to ammonia, *Adv. Mater.* 34 (2022) 1–10, <https://doi.org/10.1002/adma.202205767>.

[6] W. He, J. Zhang, S. Dieckhöfer, S. Varhade, A. Brix, A. Lielpeter, S. Seisel, J. Junqueira, W. Schuhmann, Splicing the active phases of copper/cobalt-based catalysts achieves high-rate tandem electroreduction of nitrate to ammonia, *Nat. Commun.* 13 (1) (2022) 13, <https://doi.org/10.1038/s41467-022-28728-4>.

[7] H. Niu, Z. Zhang, X. Wang, X. Wan, C. Shao, Y. Guo, Theoretical insights into the mechanism of selective nitrate-to-ammonia electroreduction on single-atom catalysts, *Adv. Funct. Mater.* 31 (2021) 2008533, <https://doi.org/10.1002/adfm.202008533>.

[8] Y. Wang, W. Zhou, R. Jia, Y. Yu, B. Zhang, Unveiling the activity origin of a copper-based electrocatalyst for selective nitrate reduction to ammonia, *Angew. Chem. Int. Ed.* 132 (2020) 5388–5392, <https://doi.org/10.1002/ange.201915992>.

[9] Q. Hu, Y. Qin, X. Wang, H. Zheng, K. Gao, H. Yang, P. Zhang, M. Shao, C. He, Grain boundaries engineering of hollow copper nanoparticles enables highly efficient ammonia electrosynthesis from nitrate, *CCS Chem.* 4 (2022) 2053–2064, <https://doi.org/10.31635/ccschem.021.202101042>.

[10] R. Wang, C. He, W. Chen, C. Zhao, J. Huo, Rich B active centers in Penta-B₂C as high-performance photocatalyst for nitrogen reduction, *Chin. Chem. Lett.* 32 (2021) 3821–3824, <https://doi.org/10.1016/j.ccl.2021.05.024>.

[11] P. Yang, H. Guo, H. Wu, F. Zhang, J. Liu, M. Li, Y. Yang, Y. Cao, G. Yang, Y. Zhou, Boosting charge-transfer in tuned Au nanoparticles on defect-rich TiO₂ nanosheets for enhancing nitrogen electroreduction to ammonia production, *J. Colloid Interface Sci.* 636 (2023) 184–193, <https://doi.org/10.1016/j.jcis.2023.01.002>.

[12] P. Yang, H. Guo, F. Zhang, Y. Zhou, X. Niu, In-situ characterization technique in electrocatalytic nitrogen reduction to ammonia, *Chin. Sci. Bull.* 67 (2022) 2921–2936, <https://doi.org/10.1360/TB-2022-0139>.

[13] Y. Wang, M. Batmunkh, H. Mao, H. Li, B. Jia, S. Wu, D. Liu, X. Song, Y. Sun, T. Ma, Low-overpotential electrochemical ammonia synthesis using BiOCl-modified 2D titanium carbide MXene, *Chin. Chem. Lett.* 33 (2022) 394–398, <https://doi.org/10.1016/j.clet.2021.05.025>.

[14] H. Guo, M. Li, Y. Yang, R. Luo, W. Liu, F. Zhang, C. Tang, G. Yang, Y. Zhou, Self-supported Pd nanorod arrays for high-efficient nitrate electroreduction to ammonia, *Small* 19 (2023) 2207743, <https://doi.org/10.1002/smll.202207743>.

[15] S. Han, H. Li, T. Li, F. Chen, R. Yang, Y. Yu, B. Zhang, Ultralow overpotential nitrate reduction to ammonia via a three-step relay mechanism, *Nat. Catal.* 6 (2023) 402–414, <https://doi.org/10.1038/s41929-023-00951-2>.

[16] Z. Niu, S. Fan, X. Li, J. Duan, A. Chen, Interfacial engineering of CoMn₂O₄/NC induced electronic delocalization boosts electrocatalytic nitrogen oxyanions reduction to ammonia, *Appl. Catal. B* 322 (2023) 122090, <https://doi.org/10.1016/j.apcatb.2022.122090>.

[17] T. Jeon, Z. Wu, F. Chen, W. Choi, P. Alvarez, H. Wang, Cobalt-copper nanoparticles on three-dimensional substrate for efficient ammonia synthesis via electrocatalytic nitrate reduction, *J. Phys. Chem. C* 126 (2022) 6982–6989, <https://doi.org/10.1021/acs.jpcc.1c10781>.

[18] Z. Deng, C. Ma, Z. Li, Y. Luo, L. Zhang, S. Sun, Q. Liu, J. Du, Q. Lu, B. Zheng, X. Sun, High-efficiency electrochemical nitrate reduction to ammonia on a Co₃O₄ nanoarray catalyst with cobalt vacancies, *ACS Appl. Mater. Interfaces* 14 (2022) 46595–46602, <https://doi.org/10.1021/acsami.2c12772>.

[19] Z. Fang, Z. Jin, S. Tang, P. Li, P. Wu, G. Yu, Porous two-dimensional iron-cyano nanosheets for high-rate electrochemical nitrate reduction, *ACS Nano* 16 (2022) 1072–1081, <https://doi.org/10.1021/acsnano.1c08814>.

[20] Y. Wang, H. Li, W. Zhou, X. Zhang, B. Zhang, Y. Yu, Structurally disordered RuO₂ nanosheets with rich oxygen vacancies for enhanced nitrate electroreduction to ammonia, e202202604, *Angew. Chem. Int. Ed.* 61 (2022), <https://doi.org/10.1002/anie.202202604>.

[21] N. Zhang, J. Shang, X. Deng, L. Cai, R. Long, Y. Xiong, Y. Chai, Governing interlayer strain in bismuth nanocrystals for efficient ammonia electrosynthesis from nitrate reduction, *ACS Nano* 16 (2022) 4795–4804, <https://doi.org/10.1021/acsnano.2c00101>.

[22] Z. Deng, C. Ma, X. Fan, Z. Li, Y. Luo, S. Sun, D. Zheng, Q. Liu, J. Du, Q. Lu, B. Zheng, X. Sun, Construction of CoP/TiO₂ nanoarray for enhanced electrochemical nitrate reduction to ammonia, *Mater. Today Phys.* 28 (2022) 100854, <https://doi.org/10.1016/j.mtphys.2022.100854>.

[23] X. Li, P. Shen, X. Li, D. Ma, K. Chu, Sub-nm RuO_x clusters on Pd metallene for synergistically enhanced nitrate electroreduction to ammonia, *ACS Nano* 17 (2022) 1081–1090, <https://doi.org/10.1021/acsnano.2c07911>.

[24] J. Li, G. Zhan, J. Yang, F. Quan, C. Mao, Y. Liu, B. Wang, F. Lei, L. Li, A. Chan, L. Xu, Y. Shi, Y. Du, W. Hao, P. Wong, J. Wang, S. Dou, L. Zhang, J. Yu, Efficient ammonia electrosynthesis from nitrate on strained ruthenium nanoclusters, *J. Am. Chem. Soc.* 142 (2020) 7036–7046, <https://doi.org/10.1021/jacs.0c00418>.

[25] E. Lacasa, P. Canizares, J. Llanos, M. Rodrigo, Effect of the cathode material on the removal of nitrates by electrolysis in non-chloride media, *J. Hazard. Mater.* 213–214 (2012) 478–484, <https://doi.org/10.1016/j.jhazmat.2012.02.034>.

[26] J. Ding, W. Li, Q. Zhao, K. Wang, Z. Zheng, Y. Gao, Electroreduction of nitrate in water: role of cathode and cell configuration, *Chem. Eng. J.* 271 (2015) 252–259, <https://doi.org/10.1016/j.cej.2015.03.001>.

[27] Z. Wu, M. Karamad, X. Yong, Q. Huang, D. Cullen, P. Zhu, C. Xia, Q. Xiao, M. Shakouri, F. Chen, J. Kim, Y. Xia, K. Heck, Y. Hu, M. Wong, Q. Li, I. Gates, S. Siahrostami, H. Wang, Electrochemical ammonia synthesis via nitrate reduction on Fe single atom catalyst, *Nat. Commun.* 12 (1) (2021) 10, <https://doi.org/10.1038/s41467-021-23115-x>.

[28] H. Yin, Y. Peng, J. Li, Electrocatalytic reduction of nitrate to ammonia via a Au/Cu single atom alloy catalyst, *Environ. Sci. Technol.* 57 (2023) 3134–3144, <https://doi.org/10.1021/acs.est.2c07968>.

[29] H. Hirakawa, M. Hashimoto, Y. Shiraishi, T. Hirai, Selective nitrate-to-ammonia transformation on surface defects of titanium dioxide photocatalysts, *ACS Catal.* 7 (2017) 3713–3720, <https://doi.org/10.1021/acscatal.7b00611>.

[30] D. Butcher, A. Gewirth, Nitrate reduction pathways on Cu single crystal surfaces: effect of oxide and Cl[−], *Nano Energy* 29 (2016) 457–465, <https://doi.org/10.1016/j.nanoen.2016.06.024>.

[31] G. Dima, A. Vooys, M. Koper, Electrocatalytic reduction of nitrate at low concentration on coinage and transition-metal electrodes in acid solutions, *J. Electroanal. Chem.* 554–555 (2003) 15–23, [https://doi.org/10.1016/S0022-0728\(02\)01443-2](https://doi.org/10.1016/S0022-0728(02)01443-2).

[32] Y. Liao, H. Xu, Z. Li, L. Ji, L. Wang, G. Gao, W. Huang, Z. Qu, N. Yan, Boosting RuO₂ surface reactivity by Cu active sites over Ru/Cu-SSZ-13 for simultaneous catalytic oxidation of CO and NH₃, *J. Phys. Chem. C* 125 (2021) 17031–17041, <https://doi.org/10.1021/acs.jpcc.1c04100>.

[33] K. Xu, Z. Ren, C. Li, Progress in application of rare metals in superalloys, *Rare Met.* 33 (2014) 111–126, <https://doi.org/10.1007/s12598-014-0256-9>.

[34] Y. Zheng, Y. Jiao, A. Vasileff, S. Qiao, The hydrogen evolution reaction in alkaline solution: from theory, single crystal models, to practical electrocatalysts, *Angew. Chem. Int. Ed.* 57 (2018) 7568–7579, <https://doi.org/10.1002/anie.201710556>.

[35] T. Li, C. Tang, H. Guo, H. Wu, C. Duan, H. Wang, F. Zhang, Y. Cao, G. Yang, Y. Zhou, In situ growth of Fe₂O₃ nanorod arrays on carbon cloth with rapid charge transfer for efficient nitrate electroreduction to ammonia, *ACS Appl. Mater. Interfaces* 14 (2022) 49765–49773, <https://doi.org/10.1021/acsmi.2c14215>.

[36] J. Li, X. Zhang, T. Wang, Y. Zhao, T. Song, L. Zhang, X. Cheng, Construction of layered hollow Fe₃O₄/Fe_{1-x}S@MoS₂ composite with enhanced photo-fenton and adsorption performance, *J. Environ. Chem. Eng.* 8 (2020) 103762, <https://doi.org/10.1016/j.jece.2020.103762>.

[37] Z. Nie, L. Zhang, X. Ding, M. Cong, F. Xu, L. Ma, M. Guo, M. Li, L. Zhang, Catalytic kinetics regulation for enhanced electrochemical nitrogen oxidation by Ru-nanoclusters-coupled Mn₃O₄ catalysts decorated with atomically dispersed Ru atoms, *Adv. Mater.* 34 (2022) 1–8, <https://doi.org/10.1002/adma.202108180>.

[38] Y. Pi, Z. Qiu, Y. Sun, H. Ishii, Y. Liao, X. Zhang, H. Chen, H. Pang, Synergistic mechanism of sub-nanometric Ru clusters anchored on tungsten oxide nanowires for high-efficient bifunctional hydrogen electrocatalysis, *Adv. Sci.* 10 (2023) 1–8, <https://doi.org/10.1002/advs.202206096>.

[39] K. Chen, Y. Luo, P. Shen, X. Liu, X. Li, X. Li, K. Chu, Boosted nitrate electroreduction to ammonia on Fe-doped SnS₂ nanosheet arrays rich in S-vacancies, *Dalton Trans.* 51 (2022) 10343–10350, <https://doi.org/10.1039/d2dt01542k>.

[40] K. Wang, J. Pan, J. Hu, X. Fu, Y. Dou, H. Xian, H. Guo, J. Chen, T. Li, Deficient tin oxide nanofibers with regulated valence for efficient nitrate reduction to ammonia, *Chem. Eng. J.* 482 (2024) 148883, <https://doi.org/10.1016/j.cej.2024.148883>.

[41] Y. Li, Y. Liu, X. Liu, Y. Liu, Y. Cheng, P. Zhang, P. Deng, J. Deng, Z. Kang, H. Li, Fe-doped SnO₂ nanosheet for ambient electrocatalytic nitrogen reduction reaction, *Nano Res.* 15 (2022) 6026–6035, <https://doi.org/10.1007/s12274-022-4298-2>.

[42] L. Zhang, M. Cong, X. Ding, Y. Jin, F. Xu, Y. Wang, L. Chen, L. Zhang, A Janus Fe-SnO₂ catalyst that enables bifunctional electrochemical nitrogen fixation, *Angew. Chem. Int. Ed.* 59 (2020) 10888–10893, <https://doi.org/10.1002/anie.202003518>.

[43] W. Zhong, Z. Gong, Z. He, N. Zhang, X. Kang, X. Mao, Y. Chen, Modulating surface oxygen species via facet engineering for efficient conversion of nitrate to ammonia, *J. Energy Chem.* 78 (2023) 211–221, <https://doi.org/10.1016/j.jechem.2022.11.024>.

[44] R. Jia, Y. Wang, C. Wang, Y. Ling, Y. Yu, B. Zhang, Boosting selective nitrate electroreduction to ammonia by constructing oxygen vacancies in TiO₂, *ACS Catal.* 10 (2020) 3533–3540, <https://doi.org/10.1021/acscatal.9b05260>.

[45] Q. Chen, J. Liang, Q. Liu, K. Dong, L. Yue, P. Wei, Y. Luo, Q. Liu, N. Li, B. Tang, A. Alshehri, M. Hamdy, Z. Jiang, X. Sun, Co nanoparticle-decorated pomelo-peel-derived carbon enabled high-efficiency electrocatalytic nitrate reduction to ammonia, *ChemComm* 58 (2022) 4259–4262, <https://doi.org/10.1039/d2cc00592h>.

[46] M. Liu, Q. Mao, K. Shi, Z. Wang, Y. Xu, X. Li, L. Wang, H. Wang, Electroreduction of nitrate to ammonia on palladium-cobalt-oxygen nanowire arrays, *ACS Appl. Mater. Interfaces* 14 (2022) 13169–13176, <https://doi.org/10.1021/acsmi.1c19412>.

[47] C. Wang, F. Ye, J. Shen, K. Xue, Y. Zhu, C. Li, In situ loading of Cu₂O active sites on island-like copper for efficient electrochemical reduction of nitrate to ammonia, *ACS Appl. Mater. Interfaces* 14 (2022) 6680–6688, <https://doi.org/10.1021/acsmi.1c21691>.

[48] H. Guo, P. Yang, Y. Yang, H. Wu, F. Zhang, Z. Huang, G. Yang, Y. Zhou, Vacancy-mediated control of local electronic structure for high-efficiency electrocatalytic conversion of N₂ to NH₃, *Small* (2023) 1–11, <https://doi.org/10.1002/smll.202309007>.

[49] R. Wang, H. Liu, K. Zhang, G. Zhang, H. Lan, J. Qu, Ni(II)/Ni(III) redox couple endows Ni foam-supported Ni₂P with excellent capability for direct ammonia oxidation, *Chem. Eng. J.* 404 (2021) 126795, <https://doi.org/10.1016/j.cej.2020.126795>.

[50] J. Liu, F. Zhang, H. Wu, Y. Jiang, P. Yang, W. Zhang, H. Guo, Y. Cao, G. Yang, Y. Zhou, Efficient carrier transfer induced by Au nanoparticles for photoelectrochemical nitrogen reduction, *Sustain. Energy Fuels* 7 (2022) 883–889, <https://doi.org/10.1039/d2se01201d>.

[51] H. Wu, H. Guo, F. Zhang, P. Yang, J. Liu, Y. Yang, Z. Huang, C. Zhu, W. Wang, X. Tu, G. Yang, Y. Zhou, Enhanced localized electron density from PdCu nanoparticles loading on defective TiO₂ support for selective nitrate

electroreduction to ammonia, *J. Mater. Chem. A* 11 (2023) 22466–22477, <https://doi.org/10.1039/d3ta04155g>.

[52] P. Yan, T. Yang, M. Lin, Y. Guo, Z. Qi, Q. Luo, X. Yu, One Stone Five Birds" plasma activation strategy synergistic with Ru single atoms doping boosting the hydrogen evolution performance of metal hydroxide, *Adv. Funct. Mater.* 33 (2023) 1–10, <https://doi.org/10.1002/adfm.202301343>.

[53] B. Liu, B. Zhong, F. Li, J. Liu, L. Zhao, P. Zhang, $\text{Co}_2\text{P}/\text{CoP}$ heterostructures with significantly enhanced performance in electrocatalytic hydrogen evolution reaction: synthesis and electron redistribution mechanism, *Nano Res.* 16 (2023) (2023) 12830–12839, <https://doi.org/10.1007/s12274-023-6228-3>.

[54] F. Yao, M. Jia, Q. Yang, F. Chen, Y. Zhong, S. Chen, L. He, Z. Pi, K. Hou, D. Wang, X. Li, Highly selective electrochemical nitrate reduction using copper phosphide self-supported copper foam electrode: performance, mechanism, and application, *Water Res.* 193 (2021) 116881, <https://doi.org/10.1016/j.watres.2021.116881>.

[55] X. Lu, J. Yu, J. Cai, Q. Zhang, S. Yang, L. Gu, G. Waterhouse, S. Zang, B. Yang, S. Lu, Exclusive nitrate to ammonia conversion via boron-doped carbon dots induced surface Lewis acid sites, *Cell Rep. Phys. Sci.* 3 (2022) 100961, <https://doi.org/10.1016/j.xcrp.2022.100961>.

[56] X. Lu, H. Song, J. Cai, S. Lu, Recent development of electrochemical nitrate reduction to ammonia: a mini review, *Electrochim. Commun.* 129 (2021) 107094, <https://doi.org/10.1016/j.elecom.2021.107094>.

[57] L. Huang, L. Cheng, T. Ma, J. Zhang, H. Wu, J. Su, Y. Song, H. Zhu, Q. Liu, M. Zhu, Z. Zeng, Q. He, M. Tse, D. Yang, B. Yakobson, B. Tang, Y. Ren, R. Ye, Direct synthesis of ammonia from nitrate on amorphous graphene with near 100% efficiency, *Adv. Mater.* 35 (2023) 1–11, <https://doi.org/10.1002/adma.202211856>.

[58] R. Ge, Y. Wang, Z. Li, M. Xu, S. Xu, H. Zhou, K. Ji, F. Chen, J. Zhou, H. Duan, Selective electrooxidation of biomass-derived alcohols to aldehydes in a neutral medium: promoted water dissociation over a nickel-oxide-supported ruthenium single-atom catalyst, *Angew. Chem. Int. Ed.* 61 (2022) e202200211, <https://doi.org/10.1002/anie.202200211>.

[59] B. Chaplin, The prospect of electrochemical technologies advancing worldwide water treatment, *Acc. Chem. Res.* 52 (2019) 596–604, <https://doi.org/10.1021/acs.accounts.8b00611>.

[60] J. Sun, X. Zhang, H. Zhang, G. Ruan, X. Wang, X. Han, M. Yuan, T. Wang, H. Xu, C. Wu, Q. Wang, Copper/carbon nanotube catalysts prepared by ion-exchange/electroreduction for electrocatalytic nitrate reduction: enhanced performance and mechanism insight, *J. Electroanal. Chem.* 936 (2023) 117377, <https://doi.org/10.1016/j.jelechem.2023.117377>.

[61] W. Fu, Z. Hu, Y. Du, P. Su, Y. Su, Q. Zhang, M. Zhou, Building dual active sites $\text{Co}_3\text{O}_4/\text{Cu}$ electrode to break scaling relations for enhancement of electrochemical reduction of nitrate to high-value ammonia, *J. Hazard. Mater.* 434 (2022) 128887, <https://doi.org/10.1016/j.jhazmat.2022.128887>.

[62] X. Ding, Y. Liang, H. Zhang, M. Zhao, J. Wang, Y. Chen, Preparation of reduced Pt-based catalysts with high dispersion and their catalytic performances for NO oxidation, *Acta Phys. Chim. Sin.* 38 (2022) 1–11, <https://doi.org/10.3866/PKU.WHXB202005009>.

[63] Y. Xu, C. Cheng, J. Zhu, B. Zhang, Y. Wang, Y. Yu, Sulphur-boosted active hydrogen on copper for enhanced electrocatalytic nitrate-to-ammonia selectivity, *Angew. Chem. Int. Ed.* (2024) e202400289, <https://doi.org/10.1002/anie.202400289>.

[64] Y. Yao, S. Zhu, H. Wang, H. Li, M. Shao, A spectroscopic study of electrochemical nitrogen and nitrate reduction on rhodium surfaces, *Angew. Chem. Int. Ed.* 59 (2020) 10479–10483, <https://doi.org/10.1002/anie.202003071>.

[65] K. Chen, Z. Ma, X. Li, J. Kang, D. Ma, K. Chu, Single-atom Bi alloyed Pd metallene for nitrate electroreduction to ammonia, *Adv. Funct. Mater.* 33 (2023) 2209890, <https://doi.org/10.1002/adfm.202209890>.